

Challenges for plasma-facing components in nuclear fusion

Cite as: Matter Radiat. Extremes 4, 056201 (2019); doi: 10.1063/1.5090100

Submitted: 24 January 2019 • Accepted: 6 June 2019 •

Published Online: 21 August 2019



View Online



Export Citation



CrossMark

Jochen Linke,^{a)} Juan Du, Thorsten Loewenhoff, Gerald Pintsuk, Benjamin Spilker, Isabel Steudel, and Marius Wirtz

AFFILIATIONS

Forschungszentrum Jülich GmbH, Institut für Energie und Klimaforschung, 52425 Jülich, Germany

^{a)}Author to whom correspondence should be addressed: j.linke@outlook.com. Present address: Auf Vogelsang 48, 52066 Aachen, Germany.

ABSTRACT

The interaction processes between the burning plasma and the first wall in a fusion reactor are diverse: the first wall will be exposed to extreme thermal loads of up to several tens of megawatts per square meter during quasistationary operation, combined with repeated intense thermal shocks (with energy densities of up to several megajoules per square meter and pulse durations on a millisecond time scale). In addition to these thermal loads, the wall will be subjected to bombardment by plasma ions and neutral particles (D, T, and He) and by energetic neutrons with energies up to 14 MeV. Hopefully, ITER will not only demonstrate that thermonuclear fusion of deuterium and tritium is feasible in magnetic confinement regimes; it will also act as a first test device for plasma-facing materials (PFMs) and plasma-facing components (PFCs) under realistic synergistic loading scenarios that cover all the above-mentioned load types. In the absence of an integrated test device, material tests are being performed primarily in specialized facilities that concentrate only on the most essential material properties. New multipurpose test facilities are now available that can also focus on more complex loading scenarios and thus help to minimize the risk of an unexpected material or component failure. Thermonuclear fusion—both with magnetic and with inertial confinement—is making great progress, and the goal of scientific break-even will be reached soon. However, to achieve that end, significant technical problems, particularly in the field of high-temperature and radiation-resistant materials, must be solved. With ITER, the first nuclear reactor that burns a deuterium–tritium plasma with a fusion power gain $Q \geq 10$ will start operation in the next decade. To guarantee safe operation of this rather sophisticated fusion device, new PFMs and PFCs that are qualified to withstand the harsh environments in such a tokamak reactor have been developed and are now entering the manufacturing stage.

© 2019 Author(s). All article content, except where otherwise noted, is licensed under a Creative Commons Attribution (CC BY) license (<http://creativecommons.org/licenses/by/4.0/>). <https://doi.org/10.1063/1.5090100>

I. INTRODUCTION

The plasma-facing wall of future thermonuclear fusion reactors with magnetic confinement such as ITER or DEMO must withstand harsh loading scenarios.^{1,2} The so-called plasma–wall interaction (PWI) processes that are crucial at the interface between the hot plasma and the wall are associated with quasistationary thermal loads up to about 20 MW m^{-2} combined with short, extremely strong thermal transients up to the gigawatts per square meter range during edge-localized modes (ELMs).^{3–6} In addition, irradiation effects resulting from the plasma species and the 14 MeV neutrons have a strong impact on the integrity of the wall armor materials. Therefore, synergistic effects resulting from simultaneous thermal, plasma, and neutron wall loads must also be evaluated in complex experiments. Under reactor-relevant conditions, the following are the most serious damaging

mechanisms: thermally induced defects such as cracking and melting of the plasma-facing material (PFM); thermal fatigue damage of the joints between the PFM and the heat sink; hydrogen-induced blistering; helium-generated formation of nanosized clusters; and neutron-induced degradation of the wall armor via reduction of the thermal conductivity, embrittlement, transmutation, and activation.

Today, tungsten is considered to be the most reliable material for high-heat-flux components in future fusion reactors owing to its high melting point ($T_{\text{melt}} = 3422 \text{ °C}$) and a thermal conductivity of approximately $160 \text{ W m}^{-1} \text{ K}^{-1}$. For ITER and other large-scale confinement experiments, alternative candidate materials based on beryllium and carbon-fiber composites (CFCs) show promise. A major drawback of the application of beryllium in PFM is its relatively low melting point ($T_{\text{melt}} = 1287 \text{ °C}$).

Beside beryllium, carbon (in particular, fiber-reinforced graphite) is the most frequently used PFM in today's magnetic confinement experiments. Depending on the selected fiber type and architecture, carbon-fiber reinforced graphite can be manufactured with thermal conductivities equal to or even better than that of copper (up to about $400 \text{ W m}^{-1} \text{ K}^{-1}$). However, such an excellent thermal conductivity will degrade rapidly under the influence of energetic neutrons. In D-T-burning fusion reactors with carbon walls, tritium-containing hydrocarbon deposits are formed on all in-vessel components. This will finally result in an unacceptable tritium inventory in the fusion reactor under current licensing laws and limits. For these two reasons, carbon has been discarded as a PFM for ITER.

On the one hand, materials research for plasma-facing components (PFCs) has become of great importance owing to the construction of ITER in Cadarache, France.⁶ On the other hand, materials research activities in the inertial confinement fusion (ICF) field are still rather scarce, although urgent material solutions will be needed the closer the performance of laser- or ion-driven fusion experiments approaches break-even. There is no doubt that the development of actively cooled wall targets will benefit significantly from progress in both the magnetic and inertial confinement fusion fields. The development of new plasma scenarios, ELM-suppression techniques, etc., will expose targets to less severe conditions, and better target design (improved geometries, new materials, etc.) will benefit the field of fusion in general. The loading conditions in both scenarios are similar (especially with regard to hydrogen, helium, and neutron loads); nevertheless, transient thermal loads differ greatly depending on the selected ICF concept and the operational situation.⁷

II. LOADS ON PLASMA-FACING COMPONENTS

Materials research for magnetic confinement experiments has now been ongoing for more than 50 years; it received strong input from a number of medium-sized tokamak devices, which were operated in the 1970s quite successfully and were in urgent need of improvements in wall materials compared with bare stainless steel vessel walls. A further need for suitable materials with well-defined specifications came with the construction of the Joint European Torus (JET, at Culham, UK), which started in 1978.

Today, material specifications and loading scenarios are primarily dictated by ITER,⁸ stellarator research with new extremely powerful confinement experiments such as Wendelstein 7X, and future DEMO-type fusion reactors. The new challenges are synergistic particle and heat loads that have been unrivalled so far (see Fig. 1). Among these are very high thermal loads, both quasistationary steady-state heat loads and very intense transients due to periodic fluctuations of the plasma pressure at the plasma edge (i.e., ELMs). These conditions are associated with an effective transport barrier at the plasma edge that forms during high-confinement (H-mode) discharges. The steady-state conditions in ITER under continuous bombardment with charged particles (H and He ions, ionized impurity atoms, and electrons) and neutral particles (charge-exchange neutrals and neutrons) will reach values of 10 MW/m^2 in the strike zone of the divertor for up to about 400 s, with slow transients as high as 20 MW m^{-2} for durations up to about 10 s. In DEMO, the heat load limits will depend strongly on advances in material development, in particular with regard to the resistance to heavy neutron irradiation loads, reaching (depending on the location) values of 4–8

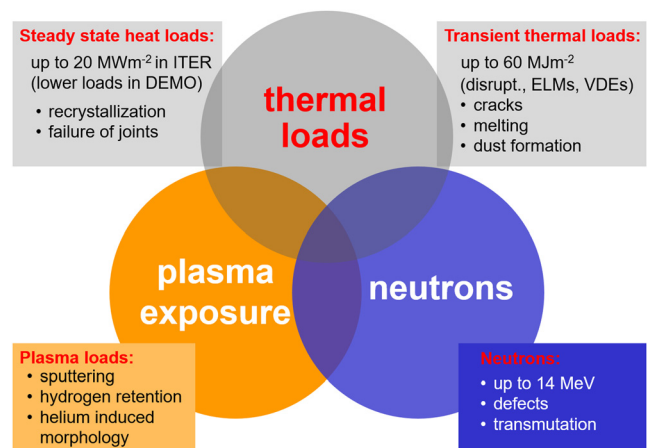


FIG. 1. Synergistic wall loads in D-T-burning magnetic confinement experiments.

displacements per atom (dpa) for the PFM and 5–15 dpa for the heat sink material during the foreseen lifetime of 1.5–2 full-power years. In comparison, in ITER, the neutron damage in the divertor will not exceed 1 dpa.

These extremely harsh loading conditions can only be met with very diligent component design and careful selection of the best suited material and manufacturing techniques. Meticulous risk assessment, nondestructive testing and the application of *in situ* diagnostics are mandatory, to validate the component lifetime and to avoid any critical deterioration of the PFM or the metallic heat sink, i.e., recrystallization of all materials and any failure of the joints due to material fatigue.

Unmitigated natural ELMs in ITER would result in serious irreversible degradation of the PFCs. Thus, thermal transients such as ELMs must remain below critical limits in terms of power density, pulse duration, and frequency.^{9–11} Therefore, mitigation technologies such as gas puffing of pellet injection must be applied continuously to trigger a higher ELM frequency, which simultaneously decreases the peak power density of each individual ELM event below the damage threshold.

Further serious lifetime-limiting PWI processes are caused by material irradiation with hydrogen isotope ions (D^+ and T^+) and impurities that—depending on their impact energy—will sputter the wall material. The eroded species will be deposited elsewhere, for example, on unshielded parts of the vacuum vessel, on blanket modules, or on less severely exposed divertor targets (outside the separatrix strike zone). Implantation of hydrogen isotopes into the surface of the PFM will result in severe embrittlement of the wall. This also has a strong impact on its cracking resistance, in particular during short transient thermal loads (i.e., ELMs). Helium will also be implanted into the surface of the wall armor or buried in redeposited surface layers. Implanted helium tends to migrate (depending on the prevailing temperature) and to form tiny bubbles that again can interact with implanted hydrogen. In several fusion-relevant PFMs (e.g., tungsten) helium can initiate rather substantial changes in surface morphology, such as the growth of tiny tendrils or “fuzz” on the surface of the PFM.¹² These layers can easily reach several micrometers in thickness. These effects need to be considered as a

potential source for the release of dust particles and contamination of the burning fusion plasma.

Finally, irradiation of wall materials by neutrons sourced from the fusion reaction produces collision cascades with high concentrations of interstitials, vacancies, and displacements, and will initiate transmutation processes. Tungsten, for example, the prime candidate for a PFM in ITER and DEMO, will transmute into rhenium (Re), which will transmute again under neutron bombardment into osmium (Os). These processes can amount to several percent of the newly generated elements.^{13,14} Consequently, alloying and property changes of the new alloy must be investigated thoroughly: rhenium can be beneficial in tungsten since it will increase its ductility, but osmium is well known as a rather brittle constituent in tungsten alloys.

The thermal wall loads that are expected for ITER in the D-T phase are envisaged to be as high as 20 MW m^{-2} on the separatrix strike point; the typical pulse length of plasma discharges will be 450 s. In addition, powerful ELMs will be triggered during the H-mode plasma operation. The natural, unmitigated ELM energy will be in the range of several tens of gigawatts per square meter, with a duration of 0.5 ms and a frequency of several hertz. These loading conditions—which will be even higher in a DEMO-type fusion reactor—will induce severe surface degradation by cracking and melting (even if tungsten is used as a PFM). Therefore, ELM-mitigation techniques have to be applied to keep the so-called heat flux factor F_{HF} below the damage threshold of about $10 \text{ MW m}^{-2} \text{ s}^{0.5}$. The heat flux factor F_{HF} represents the product of power density and the square root of pulse length Δt , which is motivated by the temperature increase of a semi-infinite body under a constant heat load.

The above-mentioned loads are visualized in Fig. 2 in a plot of power density vs duration of the prevailing event. It is important to note that both types of thermal load, namely, the quasistationary plasma discharges and the extremely short ELM-like thermal spikes, are normal operating scenarios that deposit their energy simultaneously to the divertor and other PFCs.¹⁵ Careful material selection is required to guarantee that irreversible material degradation can be excluded during long-term plasma operation of ITER.

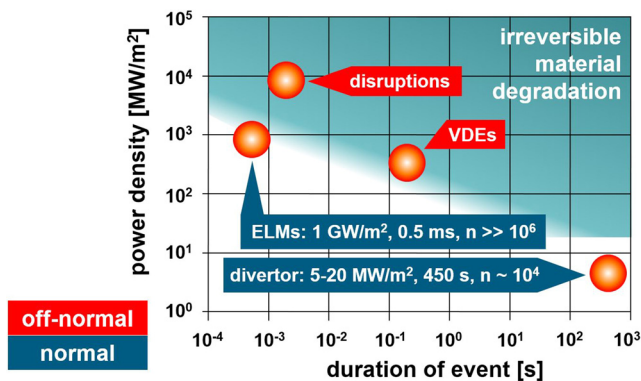


FIG. 2. Thermal loads on the divertor targets of ITER. The turquoise area represents operation conditions with irreversible material degradations during off-normal events. The irreversible damage depends on the number of pulses (for ELMs), and of course there is also degradation due to neutron and H/He loading.

In addition, off-normal plasma operation scenarios cannot be excluded completely, since ITER is an experimental plasma device that needs to explore new plasma regimes. Events such as plasma disruptions—a violent termination of the magnetically confined plasma—or vertical displacement events (VDEs)—an upward or downward motion of hot plasma due to malfunction of the plasma positioning system—may occur. The expected energy densities and pulse durations for these events depend strongly on the size of the tokamak and can be as high as 30 MJ m^{-2} for 2–5 ms (for disruptions) and up to 60 MJ m^{-2} and 100–300 ms (for VDEs) in ITER.⁹

To illustrate the interplay between steady-state heat loads and ELMs, these two effects are shown in Fig. 3 for three different plasma discharges with power densities of 5, 10, and 20 MW m^{-2} . At an ITER-specific base temperature (i.e., a coolant temperature) of $100 \text{ }^\circ\text{C}$, the surface temperature would increase to approximately 500, 900, and $1700 \text{ }^\circ\text{C}$, respectively. These conditions can be achieved with a properly manufactured monoblock-type divertor target using tungsten as an armor material and a copper alloy for the internal coolant tube (see Sec. III). Following the start-up phase of the plasma, the transition to the H-mode can be identified from the ELM activities that remain active during the full flat-top phase of the plasma discharges. In this simplified graph, an ELM intensity of $10 \text{ MW m}^{-2} \text{ s}^{0.5}$ has been assumed, which is the maximum value that can be tolerated without spontaneous deterioration such as roughening and micro-cracking of the plasma-exposed divertor target. These ELMs are responsible for an additional rise in the surface temperature of the tungsten armor of about $600 \text{ }^\circ\text{C}$, which brings the maximum surface temperature up to approximately 1100, 1500, and $2300 \text{ }^\circ\text{C}$, respectively, for the three discharges.

During a standard discharge in ITER, the maximum target temperature remains far below the T_{melt} of tungsten. However, the tungsten or tungsten alloy that has been selected for the manufacturing process will undergo substantial modifications due to recrystallization in all sections of the tungsten armor where the recrystallization temperature T_{recr} of approximately $1500 \text{ }^\circ\text{C}$ has been exceeded. It also should be mentioned that tungsten is brittle at temperatures below the so-called ductile–brittle transition temperature (DBTT), which varies

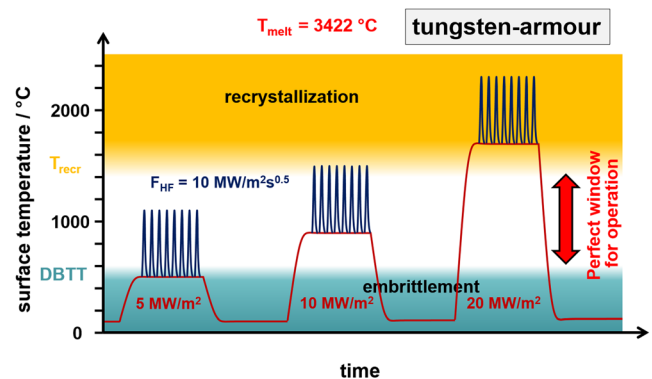


FIG. 3. Schematic presentation of the surface temperature of tungsten-armored divertor targets in ITER at three different power density levels (5, 10, and 20 MW m^{-2}). Thermal spikes caused by mitigated ELMs with an assumed intensity of $10 \text{ MW m}^{-2} \text{ s}^{0.5}$ are shown in dark blue.¹⁶ Reproduced with permission from Rieth *et al.*, *J. Nucl. Mater.* **519**, 334–368 (2019). Copyright 2019 Elsevier.

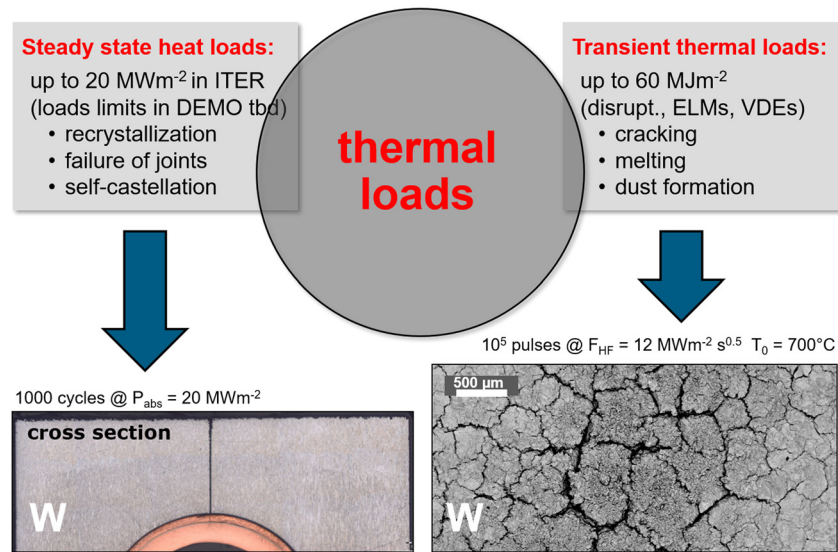


FIG. 4. Major damage to monoblock type PFCs caused by intense cyclic steady-state heat loads of 20 MW m^{-2} with 1000 pulses (left) and surface damage with intense crack networks induced by intense electron beam pulses simulating 10^5 ELM-like pulses of $F_{HF} = 12 \text{ MW m}^{-2} \text{ s}^{0.5}$ (right).¹⁷ Reprinted with permission from Pintsuk *et al.*, Fusion Eng. Des. **88**, 1858–1861 (2013). Copyright 2013 Elsevier.

in a range from approximately 200 to 600 °C, depending on the selected manufacturing processes, the related material microstructure, and the applied deformation rate.

The damaging effect on actively cooled divertor components for ITER is demonstrated in Fig. 4. Here the left-hand side of the figure shows rather serious macroscopic damage that results from cyclic thermal loads with 1000 cycles at an absorbed power density of 20 MW m^{-2} . These are typical loading conditions that are investigated in high-heat-flux experiments to simulate so-called slow transients.¹⁸ Very high thermal stresses will develop under the steep thermal gradient in a tungsten-armored monoblock tile with surface temperatures of the order of 2000 °C and an inner surface temperature of the CuCrZr coolant tube of 100 °C. This has frequently caused catastrophic failure of a tile by a deep crack that extends down to the coolant tube.¹⁷ At these very high temperatures, recrystallization of the tungsten armor is becoming the dominant lifetime-limiting parameter.¹⁹

Serious damage to the plasma-facing armor is also initiated by transient thermal loads with very high numbers of cycles: see the right-hand side of Fig. 4, where 10^5 ELM-like pulses have been applied with a heat flux factor F_{HF} of $12 \text{ MW m}^{-2} \text{ s}^{0.5}$ to a tungsten test sample preheated to 700 °C. The sample shows very intense degradation by the formation of a dense crack network at the plasma-facing surface. An assumed ITER typical ELM frequency of 25 Hz and a flat-top phase of 400 s result in 10^4 ELMs per discharge. That is, the 10^5 ELM-like pulses that have been applied in this experiment correspond to an operation time of only 10 standard plasma discharges in ITER.

III. PLASMA-FACING MATERIALS AND COMPONENTS

Several different component design options have been developed during the past few decades. The most robust and most efficient are shown schematically in Fig. 5, namely, a flat-tile design and the so-called monoblock solution. The first option consists of flat tiles that

have been machined from a PFM and are attached to a water-cooled heat sink made from a metallic alloy (the structural material) with high thermal conductivity and sufficient strength to guarantee the mechanical integrity of the full PFC. The joints between the PFM and the heat sink must provide excellent thermal contact with very high mechanical strength to avoid failures such as tile detachment (see Fig. 5, top center). This would result in local overheating of the adjacent armor tile caused by the flat incidence of the plasma particles

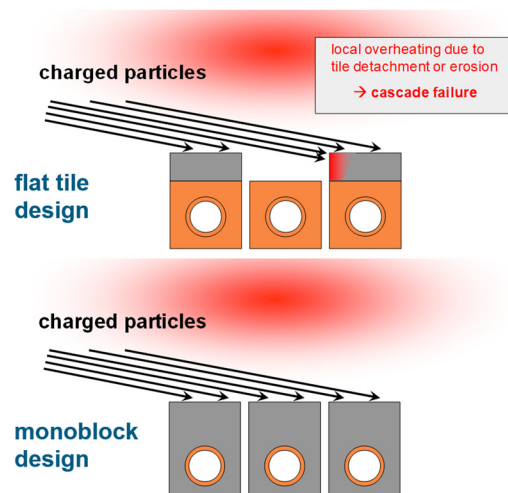


FIG. 5. Different design options for plasma-facing components in ITER. Charged particles that deposit their energy at the surface of the component are guided by the magnetic field lines at shallow angles of approximately 3° to the plasma-facing surface.

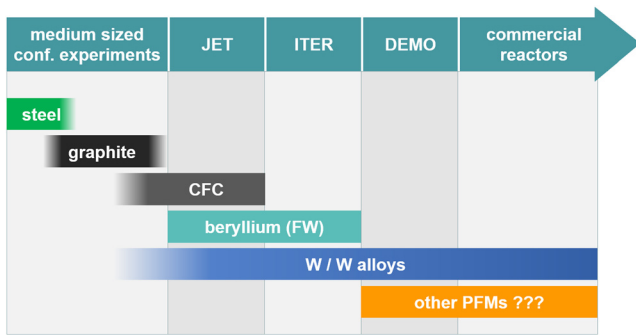


FIG. 6. Schematic summary of the implementation of new PFMs in magnetic confinement experiments. The orange bar indicates that a final decision on the use of PFMs in future fusion reactors is still pending.

that are guided by the magnetic field lines inclined at rather small angles of only a few degrees.²⁰ The loss of even a single tile is considered a rather serious event, since it would trigger overheating and degradation of joints in the adjacent tiles (so-called cascade failure).

A more robust design option is the monoblock divertor. The individual tiles of the PFM are equipped with a cylindrical hole. Rather complex joining methods such as active metal casting (AMC)²¹ and hot radial pressing²² have been developed for the joint between the PFM and the metallic coolant tube (e.g., CuCrZr or stainless steel) to remove heat and to keep the individual tiles in position, even during the conditions of an accident.

The specifications for selection of suitable PFMs are manifold: first of all, the PFM needs good compatibility with the hot fusion plasma, i.e., a low atomic number Z and an excellent sputter resistance. Alternatively, tokamaks with high- Z materials such as tungsten must be operated in such a way as to guarantee that the net impurity influx into the plasma should be so low that the critical impurity concentration is not exceeded. In addition, very high thermal conductivity, high mechanical strength, good matching of the thermal expansion coefficient

with the selected heat sink material, and low neutron-induced activation are the most critical material properties.

Early magnetic confinement experiments were performed with glass or steel walls. These material solutions turned out to be inadequate when plasma regimes with higher particle fluxes and thus higher thermal loads were achieved. In this transition phase, steel walls were replaced by carbon walls made from fine-grained graphite or pyrolytic carbon for special application with rather high thermal loads (see Fig. 6). With the operation of JET and other large tokamak devices such as TFTR (Princeton, NJ), and TORE Supra (Cadache, France), fine-grained graphite no longer provided sufficient strength and mechanical integrity to guarantee safe operation of highly exposed components in these confinement experiments. Here, carbon-fiber composites (CFCs) offered an almost ideal low- Z material to survive even the harsh environments during transients. Beside carbon, beryllium gained more and more importance as a PFM. This material guarantees plasma discharges with rather low oxygen contamination owing to its high affinity to this element. However, its toxicity, relatively low melting point ($T_{\text{melt}} = 1278\text{ }^\circ\text{C}$), and transmutation to tritium by interaction with neutrons, thereby significantly increasing the tritium inventory, are serious drawbacks that limit its applicability as a PFM for future commercial fusion reactors.

As an alternative to carbon-based materials, the high- Z material tungsten and its alloys have been successfully tested in medium-sized tokamak devices (e.g., ASDEX-U²³). These experiments have demonstrated that safe plasma operation is feasible with a full tungsten divertor. Today, tungsten divertors are securely operated also in larger confinement experiments such as WEST (Cadache, France), EAST (Hefei, China), and JET. JET, which is one of the largest existing tokamak reactors, is operated with a plasma-facing wall (the so-called ITER-like wall²⁴) consisting of a beryllium main wall and a tungsten divertor. This represents the material selection that also has been made for the ITER tokamak that is now under construction at Cadache. In ITER, the 54 modular divertor components, which weigh about 9 t each, will be fully covered with water-cooled monoblock-type tungsten for the vertical targets of the divertor

TABLE I. Different tungsten grades and alloys that have been developed and investigated thoroughly as plasma-facing and structural materials for next-step magnetic confinement experiments.

Tungsten as plasma-facing material	<ul style="list-style-type: none"> • Modification of grain structure <ul style="list-style-type: none"> ◦ Grain deformation ◦ Micro/nanostructured grains (using RSUHP, SPMM, PIM/MIM processes^a) • Smart alloys <ul style="list-style-type: none"> ◦ Re, La, Ta, K, Y₂O₃, TiC, Ti, Mo, . . . (and oxygen-resistant alloys: Si, Cr, Zr, . . .) • Tungsten coatings <ul style="list-style-type: none"> ◦ PVD, CVD, plasma spraying ◦ Functionally graded layers
Tungsten as structural material	<ul style="list-style-type: none"> • Pseudo-ductile tungsten composites <ul style="list-style-type: none"> ◦ Layered structures ◦ Fiber-reinforced tungsten

^aRSUHP, resistance sintering under ultrahigh pressure. SPMM, microstructural modification using superplasticity; PIM, power injection molding; MIM, metal injection molding.

and flat tile tungsten targets in the central dome area.²⁵ The remaining part of the inner vacuum vessel (620 m²), i.e., the first wall blanket, will be protected with 440 blanket modules with a plasma-facing surface made from bulk beryllium.²⁶ The flat tile design option will be installed with swirl tube and HyperVapotron cooling structures, depending on the expected thermal load limits (2.5 or 4.7 MW m⁻²) for the local position inside the vessel.

A major drawback of tungsten is the brittleness of this otherwise almost perfect PFM.²⁷ To improve the ductility, several new tungsten grades have been developed and tested under fusion-relevant conditions.^{24–26} These new tungsten variants are summarized in Table 1, both for applications as PFMs and for structural materials using pseudoductile tungsten composites with layered or fiber-reinforced architectures.^{28–30}

Some of these newly developed materials and manufacturing technologies, such as powder-injection molding (PIM), 3D printing, and coating by physical vapor deposition (PVD), chemical vapor deposition (CVD), or plasma spraying, also offer another attractive feature, namely, the manufacture of net-shaped tungsten parts that can be used without additional cost-intensive and time-consuming manufacturing steps. To avoid hotspots on leading edges on a segmented (or castellated) plasma-facing surface of a divertor module, the application of shaped tiles²⁰ has been proposed and is now under consideration for the ITER divertor. Some of the newly proposed technologies mentioned above, namely, PIM and 3D printing, would facilitate tile shaping considerably and would also allow the fabrication of individual tungsten tiles with 2D or 3D profiles that are optimized for local variations of the incidence angle of the magnetic field lines.

IV. TESTING OF PLASMA-FACING MATERIALS AND COMPONENTS

The selection of suitable PFMs and, in a second step, the manufacture of PFCs requires a very extensive characterization and testing procedure.³¹ For ITER and other next-step confinement experiments, all three load types described in Fig. 1, namely, high

thermal loads, hydrogen and helium bombardment, and degradation by energetic neutrons, need to be evaluated thoroughly. In this context, synergistic effects, i.e., the interactions among these load types, must be also investigated in realistic environments. In this section, a number of materials and component tests are described to summarize the state of the art in materials testing.

A. Test facilities

To simulate PWI processes in detail, many sophisticated test devices are being used in numerous laboratories worldwide. Thermal loads are simulated by intense laser or ion beams; depending on beam power and the size of the loaded area, either defocused beams or beam scanning are the most common procedures to expose large surface areas or even full PFCs. In addition, powerful linear plasma devices³² and electron beam test facilities that are extremely flexible in terms of applied power densities (quasistationary and transient) and beam shaping (temporal and lateral) are ideal test devices to simulate extreme load scenarios such as power and particle deposition in the separatrix strike zone.³³

Today, there are no adequate test devices available that would enable experiments with *in situ* neutron wall loads together with other load types (thermal and plasma loads). To mimic these conditions, high-heat-flux experiments using thermal heaters have been performed *in situ* inside the cores of nuclear fission test reactors (e.g., the HFR reactor in Petten, Netherlands,³⁴ the LVR-15 reactor in Řež, Czech Republic, and the SM-2 reactor in Dimitrovgrad, Russia³⁵). However, the irradiation rigs in these reactors offer thermal loads that are below those expected in ITER and future reactors.

Figure 7 shows a selection of test devices that are operated at Forschungszentrum Jülich and that have primarily been used for the PWI studies in this paper. In these tests, electron beam test devices turned out to be more flexible under steady-state and transient loads in a single test device. This is achieved by implementing a rather complex beam scanning algorithm with an extremely fast digital beam positioning system (1 μs per position). In addition, the smaller of the two electron beam test devices (JUDITH 1^{36,37}) with 60 kW beam

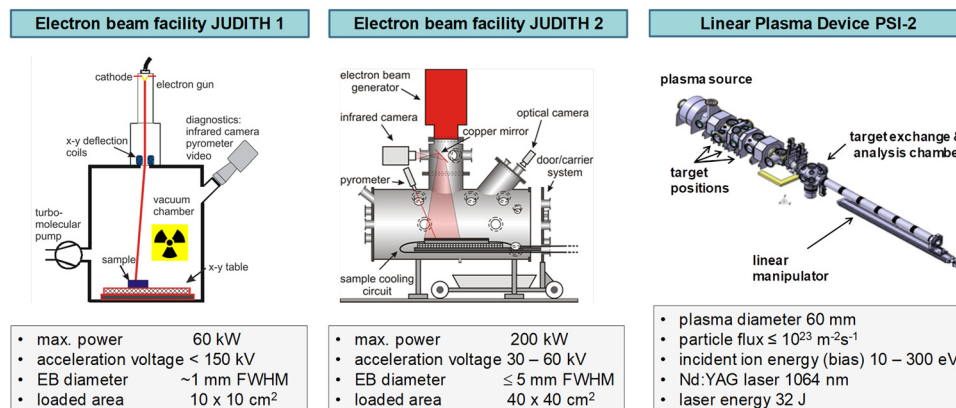


FIG. 7. Selected test facilities and layout parameters for high-heat-flux and plasma exposure of PFMs under fusion-relevant conditions that have been applied for the experiments described in this paper. A rather thin electron beam (EB) favors the simulation of transients with extreme power densities, such as plasma disruptions. Note that approximately 50% of the incident electron energy is reflected on high-Z materials such as tungsten. The electron beam facilities JUDITH 1 and JUDITH 2 are also compatible with operations with toxic materials such as beryllium, and JUDITH 1 can also handle neutron-irradiated test samples.³⁶

power is small enough to be installed inside a hot cell to perform high-heat-flux tests on neutron-irradiated materials and water-cooled components. This unique device allows high-heat-flux testing of pre-irradiated small material samples as well as actively cooled wall components with ITER- or DEMO-relevant geometries. The larger test device with a beam power of 200 kW (JUDITH 2³⁸) enables the testing of larger divertor targets with tungsten armor in fatigue mode combined with transient thermal loads that simulate ELM loads with very high repetition rates of up to 10⁶ pulses.

B. Thermal fatigue

A major threat to actively cooled PFCs comes from the high internal stresses that occur due to the thermal gradient in these components: a surface temperature of more than 2000 °C (see Fig. 3) during slow transients and an inner coolant tube temperature of, for example, 100 °C (in ITER) results in thermal gradients of about 200 K mm⁻¹. Thermal expansion and the mismatch in the coefficient of thermal expansion between the PFM and the coolant tube result in stresses that can reach values above the yield strength, leading to irreversible deformation of the component, particularly in locations close to the interface between PFM and the heat sink. This effect repeats with each thermal cycle until a complete failure of the interface can result in a rapid increase in PFC temperature and consequently in vaporization of the PFM or even complete loss of the PFM tile.

To investigate the heat load limits on different divertor designs and different armor materials, systematic high-heat-flux experiments have been performed with cyclic heat pulses at a predetermined power density level. In JUDITH 1, 1000 thermal pulses have been applied (10 s heating, 10 s cooldown). The critical parameters, namely, the surface temperature of the PFC (two-color pyrometer), the internal temperature close to the interface, and the coolant temperature (both

by thermocouples) were monitored continuously to detect sudden temperature variations initiated by internal cracks or other degradation mechanisms in the PFC.

After the successful completion of such a cyclic campaign at a predefined power density level, the heat flux density was increased to the next level (with increment typically 1 MW m⁻²). This testing procedure was applied continuously until thermal excursions indicate the occurrence of fatigue damage. Figure 8 shows the maximum power density levels that could be applied without any detectable increase in the steady state temperature initiated by microcracks or other delamination defects that can cause a deterioration in the heat flux from the plasma-facing surface to the coolant. The top row gives results for the flat tile option; the bottom row shows those for the more robust monoblock design. The vertical columns show two different armor materials that have been exposed, namely, a three-directional CFC and a bulk tungsten grade manufactured by powder metallurgy. The flat tile tungsten surface was castellated to reduce thermally induced stresses at the interface. There is clear evidence that the CFC-armored monoblock represents the most damage-tolerant solution with a fatigue damage threshold of 25 MW m⁻², followed by the tungsten monoblock with 20 MW m⁻².

It is important to note that the loading conditions that have been applied here are pure thermal fatigue conditions and do not consider any synergistic effects such as intense transients by ELM deposition, hydrogen or helium bombardment, or neutron-induced degradations (cf. Fig. 9).

C. Thermal shocks

During steady-state heat loads with pulse durations of the order of several tens of seconds or longer, the temperature field inside the PFC is characterized by an almost continuous gradient that extends

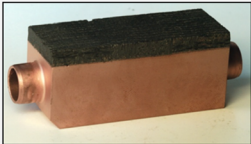
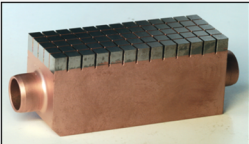
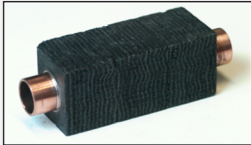
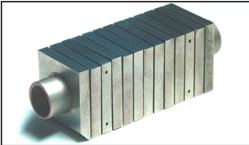
	CFC armour	tungsten armour
flat tile design	 <p>CFC flat tile Silicon doped CFC NS31, active metal casting, e-beam welding to CuCrZr heat sink 1000 cycles @ 19 MWm⁻²</p>	 <p>W macrobrush coating of WLa₂O₃ tiles with OFHC-Cu, e-beam welding to CuCrZr heat sink 1000 cycles @ 18 MWm⁻²</p>
monoblock design	 <p>CFC monoblock drilling of CFC tiles (NB31), active metal casting (AMC®) low temperature HIPing 1000 cycles @ 25 MWm⁻²</p>	 <p>W monoblock lamellae technique, drilling of WLa₂O₃ blocks, casting with OFHC-Cu, HIPing 1000 cycles @ 20 MWm⁻²</p>

FIG. 8. Thermal fatigue experiments on CFC- and tungsten-armored PFCs with design options (flat tile and monoblock). The load limits are presented in blue.

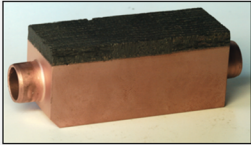
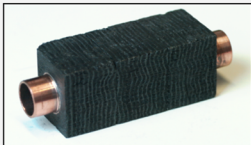
	CFC armour	tungsten armour
flat tile design	 <p>CFC flat tile 0 dpa: 1000 cycles @ 19 MWm⁻² 1 dpa: 1000 cycles @ 15 MWm⁻² (no degradation)</p>	 <p>W macrobrush 0 dpa: 1000 cycles @ 18 MWm⁻² 0.6 dpa: 1000 cycles @ 10 MWm⁻² (increasing of T_{surf})</p>
monoblock design	 <p>CFC monoblock 0 dpa: 1000 cycles @ 25 MWm⁻² 1 dpa: 1000 cycles @ 12 MWm⁻² (substantial evaporation @ 14 MWm⁻²)</p>	 <p>W monoblock 0 dpa: 1000 cycles @ 20 MWm⁻² 0.6 dpa: 1000 cycles @ 18 MWm⁻² (no degradation)</p>

FIG. 9. Thermal fatigue experiments on CFC- and tungsten-armored PFCs with different design options (flat tile and monoblock) after neutron irradiation in the HFR materials test reactor HFR in Petten at 700 °C and neutron fluxes up to 10²⁵ n m⁻². The load limits for the non-irradiated modules are shown in blue; data obtained after neutron irradiation are shown in red (see also Fig. 8).² Reprinted with permission from Linke *et al.*, in *Proceedings of Forum 2008 of the World Academy of Ceramics, Chianciano Terme, Italy, July 5–8, 2008* (Techna Group Srl, 2009), pp. 307–334. Copyright 2009 Techna Group Srl.

from the surface of the PFC down to the coolant tube. Intense transient thermal loads such as ELMs, disruptions, or VDEs with pulse durations in the millisecond range create very steep thermal gradients with a relatively shallow penetration depth that is proportional to the square root of the thermal diffusivity and the pulse duration. Hence, the damaged area during ELM-like loads will be limited to a few hundred micrometers.

Typical material damages induced by ITER-specific transient events are shown in Fig. 10 as a function of the applied energy density. VDEs and plasma disruptions are off-normal events that result in irreversible material damage such as melting and crack formation in the heat-affected zone.^{40–42} Depending on the energy density, homogeneous melting, melt ejection induced by the back pressure of the evaporated metal, or even boiling and droplet formation will make the need for replacement of the damaged component inevitable. ELMs occur regularly during H-mode discharges and must therefore be kept at power density levels that do not exceed the melting threshold. Nevertheless, even below this threshold, serious material degradations such as roughening or crack formation must be taken into consideration.⁴³ For large tokamak devices, ELM-mitigation techniques (gas puffing, pellet injection, etc.) must be applied to prevent serious wall damage.

To evaluate the resistance of different PFMs to ELM-like heat fluxes, systematic thermal load tests were performed in electron beam and laser beam experiments.⁴⁵ Figure 11 shows the results of typical electron beam experiments on pure sintered tungsten that was manufactured according to the ITER specifications by Plansee AG, Reutte, Austria. Small test specimens (12 × 12 × 5 mm³) were machined carefully to avoid any machining defects on the front surface. These tests were performed with relatively low cycle numbers (100 and 1000

electron beam pulses) of 1 ms duration. The base temperature of the samples was varied systematically in the range from room temperature to 600 °C; in addition, the absorbed power density was increased from 0.19 to 1.51 GW m⁻². Each experiment was performed on a fresh test sample that underwent a rather detailed post-mortem characterization using profilometry, scanning electron microscopy (SEM), and metallography. These tests were performed for different orientations of the grain structure (transverse and longitudinal) on forged or rolled test specimens and also on samples that had undergone a 1 h high-temperature treatment for recrystallization.

The color coding based on the above-mentioned diagnostics in Fig. 11(a) clearly shows that closed crack networks can be identified for experiments without or with only moderate preheating of the test samples ($T \leq 150$ °C). Under these conditions, tungsten is clearly below the DBTT, and the induced thermal stresses create intense crack networks. The results of tests conducted above this temperature level (the so-called “cracking threshold”) were characterized by less violent surface modifications (roughening and/or minor cracks). The “damage threshold,” i.e., the power density level below which no damage has been identified, is at 0.2 GW m⁻² for this particular tungsten grade with a longitudinal grain orientation. This power density level corresponds to a heat flux factor $F_{HF} = 6$ MW m⁻² s^{0.5} (=power density multiplied by square root of duration).

Figure 11(b) shows typical SEM images from the load surface and from cross sections (optical microscopy) for two different grain orientations and for recrystallized material. In electron beam tests performed at room temperature and a power density of 0.38 GW m⁻², a characteristic surface crack pattern developed after only 100 pulses for each of the three test samples. These cracks follow the grain boundaries and are very representative of the microstructure of the test

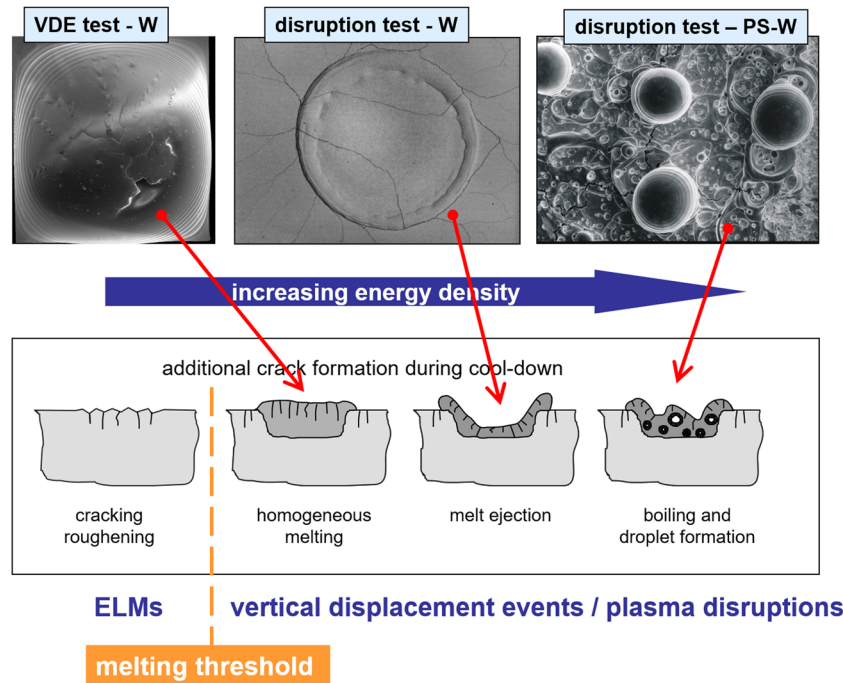


FIG. 10. Schematic presentation of the degradation of tungsten-based armor tiles with increasing transient thermal loads below and above the melting threshold.³⁹ The top row shows photographs from test samples that have been exposed to off-normal events that might occur in ITER if suitable mitigation techniques are not applied.

specimens. The mean crack depth shows its lowest values for the longitudinal grain orientation ($\sim 100 \mu\text{m}$), increases to $\sim 200 \mu\text{m}$ for the transverse orientation, and is even larger ($\sim 300 \mu\text{m}$) for the recrystallized material.

The experimental procedure described above has been applied to a large number of metallic PFMs, primarily to tungsten- and beryllium-based materials. In addition, alloys of high-Z metals, materials with modified grain structures, and coatings made from

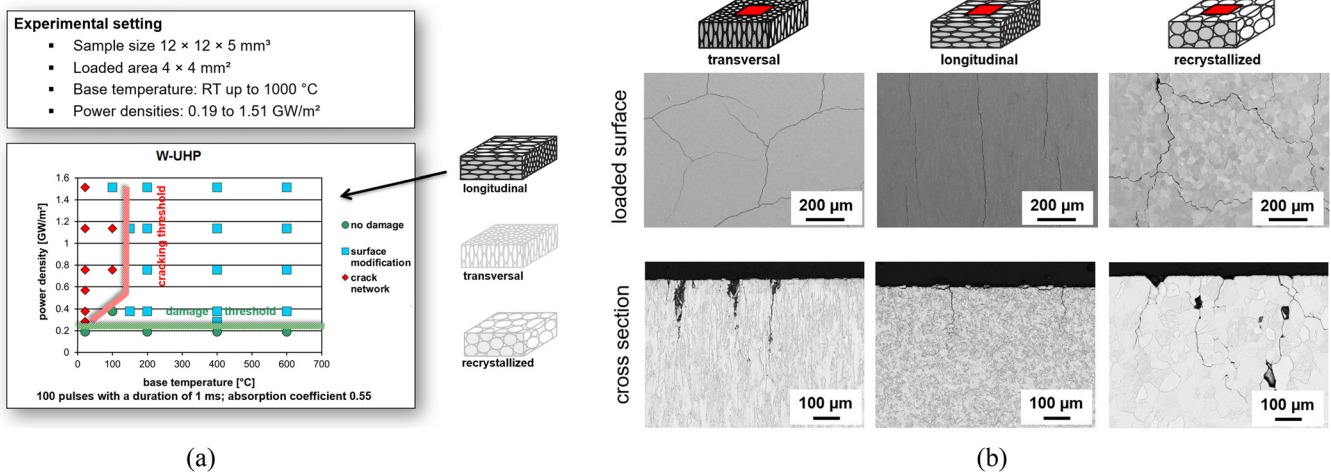


FIG. 11. (a) Generation of a typical damage map for an ultra-high-purity (UHP) tungsten grade with longitudinal grain orientation under intense transient thermal loads applied in the electron beam test facility JUDITH 1. Each data point represents a single test sample that has been exposed to 100 electron beam pulses at different base temperatures and power density levels (green circles, no damage; blue squares, surface modifications; red diamonds, crack network).⁴⁴ Reprinted with permission from Wirtz *et al.*, Nucl. Mater. Energy **12**, 148–155 (2017). Copyright 2017 Elsevier. (b) Micrographs taken by scanning electron microscopy (top row) and after metallographic sectioning using optical microscopy (bottom row) on tungsten test samples exposed to one particular load scenario plotted in the damage map in (a). The three different test specimens (transverse, longitudinal, and recrystallized) have been exposed to 100 repeated electron beam pulses under identical conditions: a power density level $L_{\text{abs}} = 0.38 \text{ GW m}^{-2}$ ($F_{\text{HF}} = 12 \text{ MW m}^{-2} \text{ s}^{0.5}$) and a base temperature $T_{\text{base}} = \text{room temperature}$.⁴⁴

these materials have been tested. With a beam repetition rate of 1 s to allow sample cool-down in between shots and to accommodate the large number of samples required to develop the damage mapping, this procedure turned out to be rather time-consuming in JUDITH 1 for experimental campaigns with more than 1000 pulses (namely, ~20 min for 1000 pulses, or 280 h for 10^6 electron beam pulses per data point).

To overcome this problem with the low repetition rate, the more powerful electron beam device JUDITH 2 has been operated with an upgraded digital beam control system which allows the programming of rather complex beam traces on the surface of actively cooled PFCs. Active cooling is mandatory for these tests to avoid excessive heating of the loaded surface and, in addition, to combine the transient thermal loading with steady-state heat loads that provide the base temperature (e.g., 700 °C for an experiment with a steady-state heat flux of 10 MW m^{-2}). These tests [see Fig. 12(a)] have been performed with a pulse duration of 0.48 ms and a simulated ELM frequency $f_{\text{ELM}} = 25 \text{ Hz}$. This method allows the investigation of pulse numbers up to 10^6 in less than 12 h machine time.

The damage map in Fig. 12(a) shows [in analogy to Fig. 11(a)] the resulting damage on small test specimens made from bulk tungsten with a longitudinal surface orientation. These samples have been brazed to water-cooled support structures. The diagram uses the same damage codes as Fig. 11(a); however, here the ordinate shows the pulse number on a logarithmic scale instead of the base temperature. All experiments summarized in this map were performed at a constant surface temperature of 700 °C (controlled by a two-color pyrometer) as described above. Results from JUDITH 1 experiments performed at heat flux factors of 9 and 12 $\text{MW m}^{-2} \text{ s}^{0.5}$, respectively, with very low pulse numbers ($n = 10$ and 100) are also included.

This map demonstrates clearly that experiments conducted at a given heat flux factor (e.g., $F_{\text{HF}} = 9 \text{ MW m}^{-2} \text{ s}^{0.5}$) show growing

damage with increasing pulse number. Small cracks (seen after 100 cycles) develop into crack networks and melting effects [visible after 10^5 pulses; see the micrographs in Fig. 12(b)]. Another effect is important to note: reducing the power density of the electron beam delays the damaging process considerably. For a heat flux factor of $6 \text{ MW m}^{-2} \text{ s}^{0.5}$, crack networks become visible only after 10^6 pulses. For $F_{\text{HF}} = 3 \text{ MW m}^{-2} \text{ s}^{0.5}$, the power is below the damage threshold, and the plasma-facing surface remains unaffected.

As a conclusion for next-step tokamaks including ITER, the heat flux factor should remain below $6 \text{ MW m}^{-2} \text{ s}^{0.5}$ to avoid component failure due to high-cycle fatigue induced by frequent ELM events. It is important to note that these results do not yet include any synergistic effects induced by hydrogen, helium, or neutron bombardment.

Thermally induced cracking or opening of grain boundaries in the plasma-facing surface can be a hazard for the safe operation of a confinement device: deep cracks have a strong impact on heat removal through the PFM into the heat sink. In particular, cracks that are oriented perpendicular to the thermal gradient in the armor material show reduced capability for heat removal and end up in isolated hot-spots that even reach temperatures above the melting point of tungsten. An example of this effect is shown in Fig. 12(b). The SEM image shows the corrugated surface layer together with a cross section from a major crack with secondary cracks oriented parallel to the surface and isolated molten grains. These tiny re-solidified objects are also visible in the SEM image taken from the surface (droplet size ~ 10–30 μm). The formation of liquid tungsten is a major concern for safe plasma operation, since critical contaminations of the plasma with high-Z materials could trigger dangerous plasma disruptions.

From this point of view, carbon is a much more “forgiving” material than tungsten or other metals. The absence of any liquid phase on carbon-armored PFCs and the very low atomic number of carbon eliminate the risk of large melt accidents during off-normal

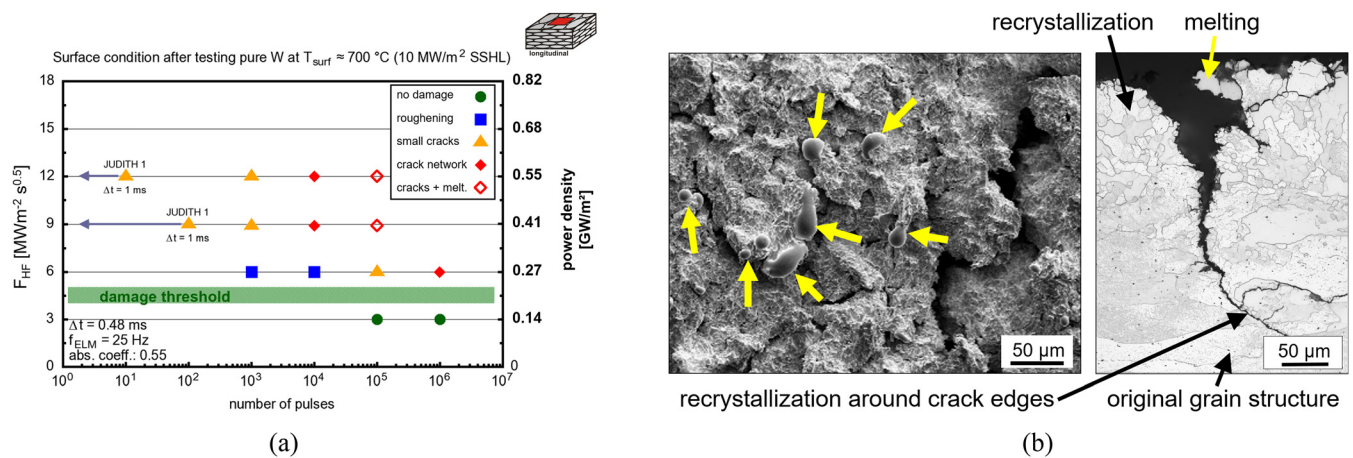


FIG. 12. (a) Damage map for actively cooled tungsten specimens under simultaneous steady-state heat loads (SSHL = 10 MW m^{-2}) and intense transient thermal loads applied in electron beam tests with high repetition rates (25 Hz) and an absorption coefficient on tungsten targets of 0.55. The chart summarizes experimental data that have been taken at different power density levels for the transient events and pulse numbers up to $n = 10^6$ and at a constant base temperature $T_{\text{surf}} = 700 \text{ °C}$.⁴⁶ Reprinted with permission from Loewenhoff *et al.*, Phys. Scr. **T145**, 014057 (2011). Copyright 2011 IOP Publishing. (b) Results from post-mortem analyses on a tungsten test sample that has been exposed to 10^5 transient thermal load pulses in the damage map in (a). The tests were performed at a heat flux factor $F_{\text{HF}} = 9 \text{ MW m}^{-2} \text{ s}^{0.5}$ and a base temperature $T_{\text{surf}} = 700 \text{ °C}$. The surface is covered homogeneously with a high number of re-solidified tungsten droplets that are generated when individual tungsten grains are thermally isolated by thermal shock-induced microcracks.⁴⁷ Reprinted with permission from Loewenhoff *et al.*, Fusion Eng. Des. **87**, 1201–1205 (2012). Copyright 2012 Elsevier.

events such as VDEs or major plasma disruptions. Therefore, in earlier stages of the ITER design phase, CFCs were proposed as armor for the very high-heat-flux regions of the divertor, i.e., for the separatrix strike zone and adjacent targets. The very high thermal conductivity of CFCs with pitch fiber reinforcement led to excellent thermal shock resistance with almost twice the values that could be realized in high-dense tungsten grades.

Carbon-based materials are no longer PFM candidates in ITER, because of their high tritium retention. However, they excel in heat load tests and are therefore discussed in what follows. Transient heat load tests on CFCs confirmed their high resistance against erosion of the pitch fibers to intense ELM-like loads with energy densities of up to 1.0 MJ m^{-2} at pulse durations of 0.5 ms ($F_{\text{HF}} = 44.7 \text{ MW m}^{-2} \text{ s}^{0.5}$). However, the polyacrylonitrile (PAN) fibers and needled PAN fibers that are responsible for the mechanical properties of these three-directional composites are heavily eroded under intense heat fluxes.⁴⁸ This is because the thermal conductivity along the carbon fiber axis is extremely high (especially for pitch fibers), but only marginal in a direction perpendicular to the fiber strands. Therefore, all PAN fibers oriented perpendicular to the heat flux direction show severe degradation, which could reach values as high as $100 \mu\text{m}$ after 100 ELM-like pulses.

A further drawback of CFC material under extreme thermal shocks is that thermally induced stresses during these thermal spikes can even destroy the fiber integrity. After 100 pulses with a heat flux factor of $31.3 \text{ MW m}^{-2} \text{ s}^{0.5}$, some of the pitch fiber bundles are completely broken; the cracks extend to a depth of $100 \mu\text{m}$ as shown in Fig. 13. This has a strong impact on the heat removal efficiency of the damaged fiber strands and bears the risk of an accidental delamination of the pre-damaged surface layers.⁴⁹ It should be noted that the cracks can only be identified in high-resolution optical micrographs; in lower magnification images such as Fig. 14, these cracks are hardly visible.

Like tungsten, carbon-based materials such as isotropic fine grain graphite also show a strong increase in damage above a certain damage threshold. Test samples were subjected to disruption-like heat pulses of 2 ms duration with stepwise increasing power densities

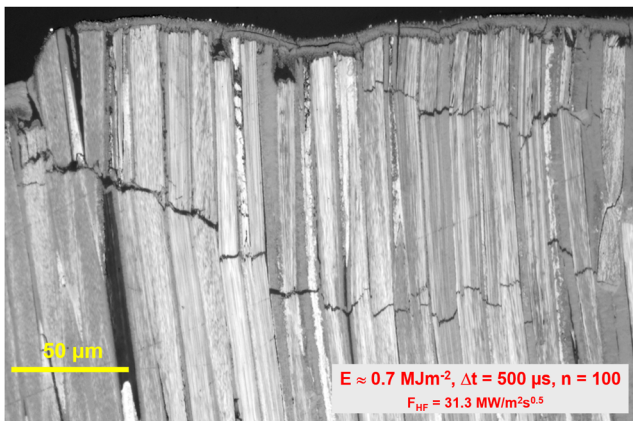


FIG. 13. Ceromographic section from a CFC sample exposed to 100 transient heat pulses with an energy density of 0.7 MJ m^{-2} , $\Delta t = 500 \mu\text{s}$ show deep cracks that intersect the pitch fiber bundles owing to thermal stresses.⁴⁸

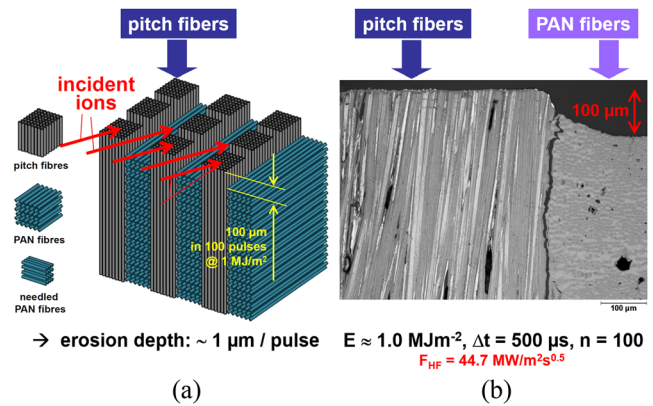


FIG. 14. View of thermal shock experiments simulating unmitigated ELMs deposited on a CFC surface: (a) schematic; (b) ceromographic section from a loaded test sample. The pitch fibers of this composite with a high thermal conductivity along the fiber axis do not show any severe thermal erosion, while the PAN fibers with an orientation parallel to the surface are strongly affected and show a total erosion of approximately $100 \mu\text{m}$.

from 3.1 to 3.3 and 4.3 GW m^{-2} (see Fig. 15). Photographs taken during these tests show the ejection of hot carbon particles (graphite grains or grain clusters) from the heat-affected graphite target. Composites with a multidirectional fiber reinforcement can reduce these accidental erosion processes significantly owing to their higher thermal conductivity and superior mechanical strength.

In addition to the divertor, other components will be subject to the heat load originating from the plasma. The armor of the blanket, i.e., the first wall that protects the breeding blanket in future tritium-burning confinement experiments, must withstand less severe thermal loads compared with the divertor target. To avoid excessive neutron absorption and thus allow for a sufficiently high tritium breeding ratio in the breeding blanket, the thickness of the high-Z armor layer must be limited to a few (2–3) millimeters only, and the structural material, including the coolant tubes, must be manufactured from a less dense material (compared with tungsten) with adequate thermal conductivity and neutron resistance, for example, steel. In addition, this component requires very sophisticated engineering to guarantee a long lifetime of the blanket modules and to avoid any contaminations of the fusion plasma from wall material that might enter the core plasma owing to delamination or evaporation processes. Tungsten, with its extremely high melting point, might also be a very suitable material for the plasma-facing wall (e.g., as a plasma-sprayed coating or a plated layer).

For ITER, the tritium-breeding blanket first wall will be made from a low-oxygen vacuum hot-pressed beryllium grade that is attached to a CuCrZr heat sink. This material selection has been motivated by the relatively high thermal conductivity of beryllium and its low atomic number, which make plasma contamination by wall material (e.g., as a result of sputtering processes) less harmful. In addition, beryllium is an excellent getter for oxygen, which enables plasma discharges with low impurity levels (i.e., so-called low-Z effective discharges). However, the toxicity of beryllium and its relatively low melting point $T_{\text{melt}} = 1278 \text{ }^\circ\text{C}$ are less favorable properties that hamper the use of this rather interesting material for applications in future fusion reactors beyond ITER.

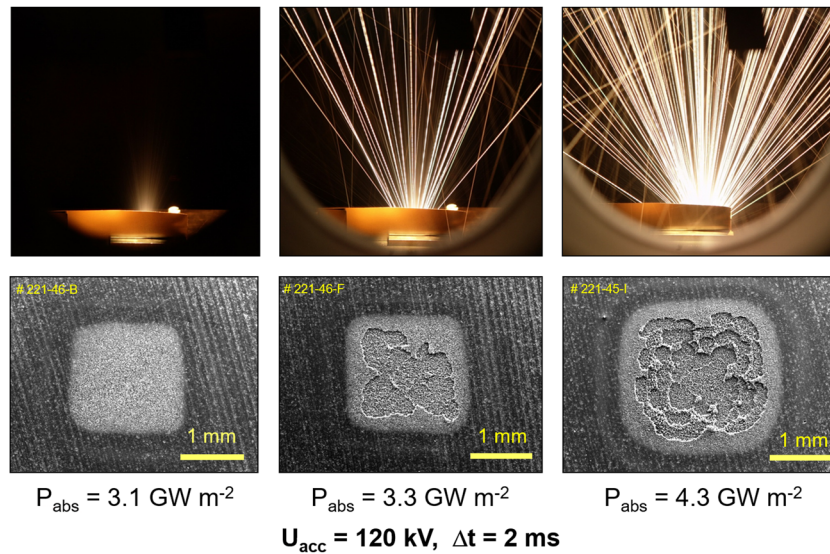


FIG. 15. Disruption simulation experiments on isotropic fine-grained graphite in the electron beam test facility JUDITH 1 with increasing power density level.⁵⁰ The top row shows long-exposure photographs taken during the 2 ms beam exposure; i.e., emitted hot particles are identified from their straight trajectories. The bottom row are SEM images from the exposed surfaces. Up to a threshold value of 3.1 GW m^{-2} , thermally induced material erosion remains marginal; above this threshold, intense emission of grains or grain clusters and intense surface erosion has been identified.⁵¹ Reprinted with permission from Linke, *Trans. Fusion Sci. Technol.* **53**, 278–287 (2008). Copyright 2008 Taylor and Francis.

The performance of beryllium under extreme transient thermal loads has been investigated thoroughly in experiments analogous to those on tungsten described above.^{53–55} Surprisingly the damage threshold for roughening and cracking (roughening threshold $F_{\text{HF}} = 6\text{--}10 \text{ MW m}^{-2} \text{ s}^{0.5}$ and cracking threshold $F_{\text{HF}} = 13\text{--}16 \text{ MW m}^{-2} \text{ s}^{0.5}$ for base temperatures of 300°C) were found to be only slightly lower than those for tungsten despite the

higher melting temperature of the latter, $T_{\text{melt}} = 3422^\circ\text{C}$. However, this is not true for the melting threshold $F_{\text{HF}} = 22\text{--}25 \text{ MW m}^{-2} \text{ s}^{0.5}$, which is at least a factor of two smaller than that of tungsten. As demonstrated above for tungsten, high-cycle fatigue effects are also very important for metallic PFMs. Figure 16 shows such an effect for polished beryllium test samples that had been exposed to disruption-like transient electron beam pulses ($\Delta t = 5 \text{ ms}$) with

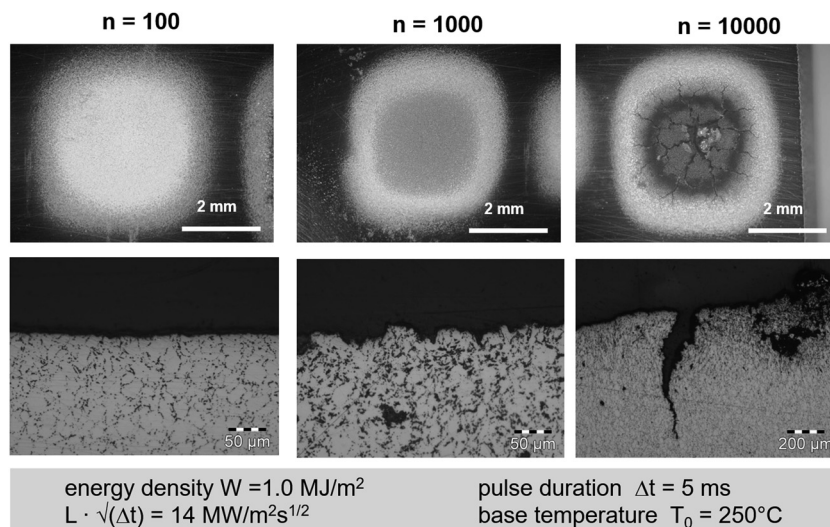


FIG. 16. Repeated disruption-like electron beam loads ($\Delta t = 5 \text{ ms}$) on polished beryllium test specimens preheated to 250°C . Up to 100 pulses, the surface (top row, SEM images; bottom row, metallographic sections) does not exhibit any erosion; intense surface roughening is evident after 1000 pulses; intense cracks with a depth of $500 \mu\text{m}$ are detected after 10 000 pulses.⁵²

absorbed energy densities $W = 1.0 \text{ MJ m}^{-2}$, which corresponds to a heat flux factor $F_{\text{HF}} = 6\text{--}10 \text{ MW m}^{-2} \text{ s}^{0.5}$. After 100 pulses, the test specimen does not show any deterioration; however, after 1000 pulses, a clear roughening with a surface roughness of a few tens of micrometers becomes visible. After 10 000 disruption events, the heat-exposed surface shows a very dense crack network with cracks extending to a depth of approximately $500 \mu\text{m}$.

Figure 17 compares the damage thresholds for the prime PFM candidates, namely, CFCs, tungsten, and beryllium, for typical ELM or disruption-like transient loads under typical loading conditions for the divertor ($T_0 = 500^\circ\text{C}$ for CFC or tungsten; $T_0 = 200\text{--}300^\circ\text{C}$ for beryllium) and at moderate pulse numbers. For all these materials, the damage threshold was found at heat flux factors F_{HF} of approximately $10 \text{ MW m}^{-2} \text{ s}^{0.5}$. This means that large magnetic confinement experiments such as ITER, DEMO, and other future fusion reactors require effective and reliable ELM-mitigation techniques to achieve these goals.¹⁰ Very high cycle numbers and synergistic effects due to hydrogen, helium, and neutron bombardment are not included in the diagram in Fig. 17. Testing of high cycle numbers up to $n = 10^7$ on beryllium has revealed a damage saturation threshold of $F_{\text{HF}} = 9\text{--}12 \text{ MW m}^{-2} \text{ s}^{0.5}$.^{56,57}

In addition to comprehensive and costly experimental campaigns that cover individual or synergistic effects, numerical methods are important tools to aid the synthesis of new materials with improved properties, to predict the performance of complex components, to benchmark experimental findings, and to predict material performance in very complex and harsh conditions.^{58–60}

V. IRRADIATION EFFECTS

As well as extreme thermal loads, particle bombardment from the hot fusion plasma is another serious issue for wall materials in future fusion reactors. Since charged particles such as deuterium and tritium, which are guided by the magnetic field lines, have only a very shallow penetration depth, they will primarily affect the near-surface

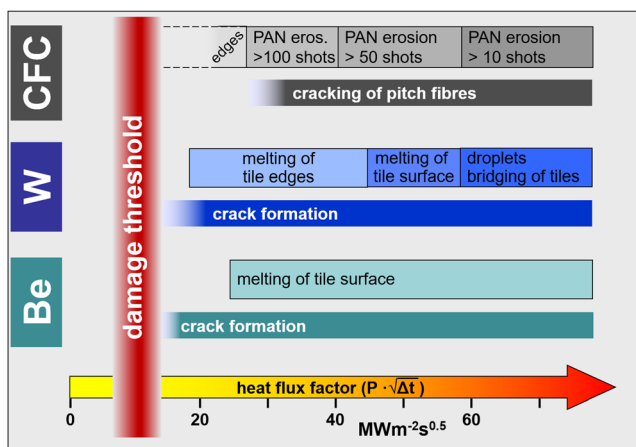


FIG. 17. Comparison of the resulting material degradation on different PFMs under repeated transient thermal loads ($n \leq 100$). Tungsten and CFC data were obtained on a quasistationary plasma accelerator (QSPA), with 0.5 ms pulse duration and $T_0 = 500^\circ\text{C}$; beryllium data were from electron beam experiments on JUDITH 1, with $T_0 = 300^\circ\text{C}$. The damage threshold values for all three materials are at a level of approximately $10 \text{ MW m}^{-2} \text{ s}^{0.5}$.^{2,40,48,54}

region of the PFM. However, owing to diffusion processes on hot walls, hydrogen ions in particular can also penetrate into deeper layers. Neutrons of energy 14 MeV have a penetration depth of up to several tens of centimeters, depending on the selected materials and the coolant. This means that neutron-induced degradation must be taken into account for the plasma-facing component as well as for structural materials.⁶¹

A. Hydrogen and helium effects

Extensive studies of hydrogen and helium bombardment have been performed in laboratories worldwide to investigate and quantify sputtering effects and microstructural changes of the bombarded surface layer, including recombination effects and migration of defects and defect clusters. As well as these single-load effects, combined events such as simultaneous bombardment with helium and hydrogen ions⁶² must be studied experimentally and numerically to quantify effects such as hydrogen trapping in helium bubbles. In addition, synergistic effects, i.e., the interaction of intense thermal loads with particle-induced degradation, have already been taken into consideration.^{63,64}

To highlight the importance of such synergies, material degradation under simultaneous helium irradiation and intense transient thermal loading using a focused laser beam is illustrated in Fig. 18. Helium bombardment of a hot tungsten surface ($T_{\text{surf}} \geq 800^\circ\text{C}$) results in substantial surface modifications of the (polished) sample surface by the growth of a dense network of tiny tendrils with diameters of several tens of nanometers. After fluences of more than $10^{25} \text{ He atoms m}^{-2}$, a porous tungsten layer forms that turns into tendrils (also called tungsten fuzz¹²) with a thickness of several micrometers [see Fig. 18(a)]. Repeated ELM-like transients generated by a Nd-YAG laser,⁶⁵ which have been applied during the growth process of the tendrils, have little impact if the heat flux factor F_{HF} of the individual ELMs remains below $6.0 \text{ MW m}^{-2} \text{ s}^{0.5}$. At higher ELM intensities [e.g., $12.0 \text{ MW m}^{-2} \text{ s}^{0.5}$; Fig. 18(c)], a significant fraction of the tungsten fuzz shows coagulation effects due to melting. After intense ELM loading [$24.0 \text{ MW m}^{-2} \text{ s}^{0.5}$; Fig. 18(d)], intense tendril growth is prevented by the immediate re-melting of the new-grown filaments. Hence, intense thermal transients can prevent the growth of low-density fuzz layers and also reduce the risk of spontaneous material delamination and subsequent plasma contamination from these layers. Nevertheless, the eroded tendrils and the remaining tungsten surface still contain a considerable fraction of helium bubbles in the near-surface region with a depth of approximately $100 \mu\text{m}$ [Fig. 18(d)].

B. Material degradation by energetic neutrons

To study neutron-induced material degradation, PFMs, structural materials, and miniaturized components have been irradiated by a number of different neutron sources such as fission-type material test reactors or spallation neutron sources. Unfortunately, the neutron spectra in these devices do not fully coincide with the fusion neutrons generated in D-T fusion reactions. The International Fusion Materials Irradiation Facility (IFMIF), with an almost perfect energy spectrum, is still in an early design stage and will not be available before 2030 (IMIF-DONES).⁶⁸ Another drawback of present-day neutron sources is that procedures that involve synergistic effects, such as high-heat-flux testing under the impact of neutron irradiation

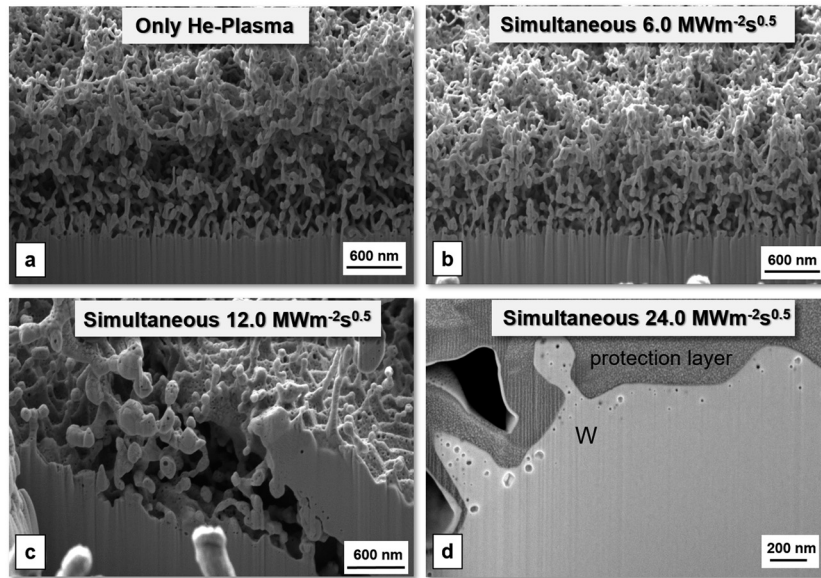


FIG. 18. Synergistic experiments with simultaneous exposure of polished tungsten specimens under helium bombardment and laser beam transient thermal loads in the PSI-2 linear plasma device.⁶⁵ Helium implantation at high temperatures initiated the growth of tiny tungsten tendrils (tungsten fuzz). SEM images were taken on sections cut with focused ion beams using Ga ions.⁶⁶ Reprinted with permission from Wirtz *et al.*, Nucl. Mater. Energy 9, 177–180 (2016). Copyright 2016 Elsevier.

in situ in a material test reactor, are technically extremely difficult and are limited to relatively low neutron fluences owing to early failure of the irradiation rig.³⁵

Post-irradiation testing (PIE) following well-instrumented irradiation experiments in material test reactors has been performed on all fusion-relevant PFMs with ITER-relevant fluences up to 1.0 dpa in carbon (approximately $10^{25} n m^{-2}$). These irradiation tests require a very diligent design and construction of the irradiation capsule, with heaters or coolant channels to guarantee the predetermined irradiation temperature.

Heat removal from plasma-facing components from the heat-affected surface to the coolant is strongly determined by the thermal conductivity λ of the PFM and the heat sink. During neutron irradiation, energetic neutrons with energies of up to 14.7 MeV generate collision cascades. During their decay process, a large fraction of point defects and interstitials are generated, which have strong impact on the thermal conductivity. The neutron-induced decrease in λ of the full PFC is a serious concern for the safe operation of a reactor, since increasing surface temperatures of the PFC surfaces will in turn affect the recrystallization of the PFM.

Cylindrical test specimens, manufactured from different grades of PFM and with different surface orientations were irradiated in material test reactors at different temperatures (200–700 °C) up to neutron damage rates of 1.0 dpa. A thermal flash apparatus installed inside a hot cell was utilized to measure the thermal diffusivity and thus (after multiplication by temperature-dependent data for density and specific heat) the thermal conductivity.⁵⁰ These data have been compared with measurements on un-irradiated test samples made from identical materials; see Fig. 19.

CFCs show excellent thermal conductivities, one reason why they have been considered as excellent PFMs for the separatrix strike

zone of next-step fusion devices with moderate neutron fluences. Nevertheless, the values of the thermal conductivity λ determined after 0.1 dpa already show a very drastic decrease, especially at low temperatures. For neutron fluences expected at the end of life of ITER (approximately 1 dpa) the effect is even stronger, and the room-temperature thermal conductivity is decreased by almost one order of magnitude.

For tungsten, the degradation of the thermal conductivity is less severe; here the neutron-induced decrease in λ is limited to about 25%–30% at low temperatures and diminishes at elevated temperatures above 1000 °C. This is a strong argument for the selection of tungsten as a PFM for ITER and especially for future fusion reactors with very high neutron fluences. However, it must be noted that reliable irradiation data for relevant neutron damages of up to 8 dpa for DEMO are not yet available.

Experiments exploring the performance of neutron-irradiated PFMs can only be done in a hot cell to protect the operators from high radioactivity of the neutron-irradiated specimens or actively cooled components.⁶⁹ To this end, the JUDITH 1 facility (Fig. 7) can be operated fully by manipulators and remote techniques. With a 60 kW electron beam gun that can be operated in scanned or focused mode, both quasistationary and transient regimes can be simulated. Sophisticated diagnostics for the measurement of temperatures (infrared scanner and thermocouples), flow rates, etc., are installed inside the vacuum chamber [see Fig. 20(a)].

Figure 20(b) shows the steady-state surface temperature of the plasma-facing surface during the so-called screening experiments in the electron beam test facility JUDITH 1, plotted as a function of the absorbed thermal load. The blue squares represent data taken from the un-irradiated monoblock-type PFC, and the red circles represent data from the same component after neutron irradiation in the HFR

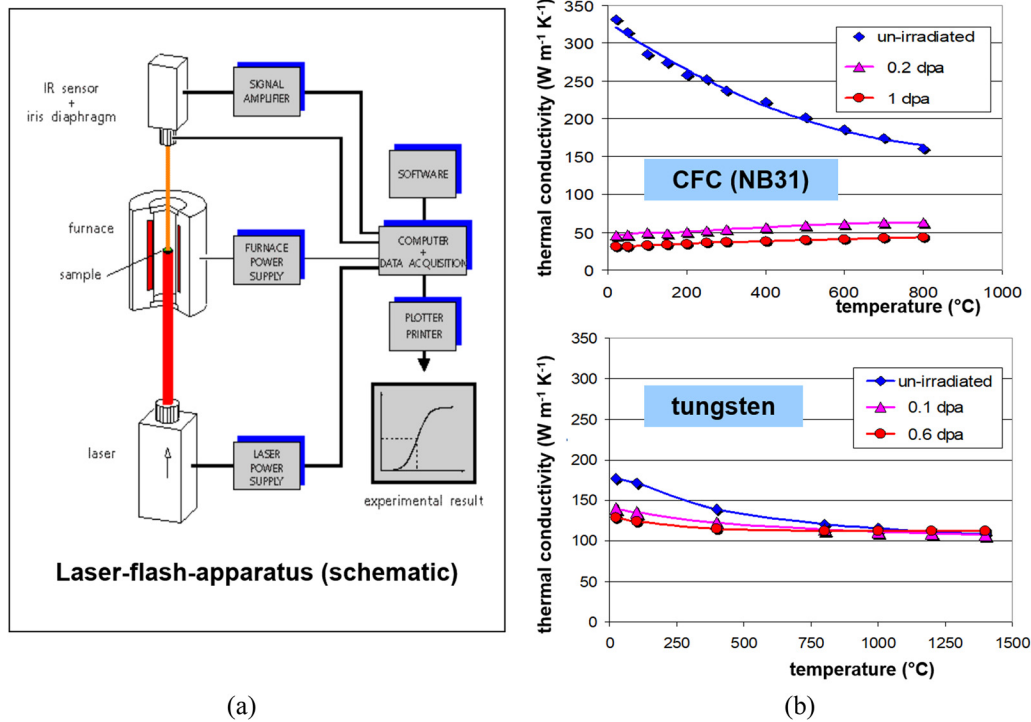


FIG. 19. (a) Schematic presentation of the laser-flash apparatus used to determine the thermal diffusivity. (b) Thermal conductivity data measured on a CFC (NB31) and a tungsten specimen without and after neutron irradiation at neutron damage rates up to 1.0 dpa for carbon and 0.6 dpa for tungsten.⁷¹ Reprinted with permission from Linke *et al.*, Fusion Sci. Technol. **47**(3), 678 (2005). Copyright 2005 Taylor and Francis.

reactor at Petten. The full PFC has been irradiated at $T_{irr} = 350^{\circ}C$ with a damage rate of 0.3 dpa (in carbon).⁵⁰

Owing to the hexagonal lattice structure of graphite, neutron-induced defects are produced in a basal plane and/or in-between the basal planes.⁷⁰ These defects can recover easily at elevated temperatures (above 800–1000 $^{\circ}C$); i.e., lightly irradiated graphite can recover

its initial thermal conductivity values by annealing far below the graphitization temperature.

The unirradiated component has been tested up to stationary heat loads of 25 $MW m^{-2}$; the surface temperature increases almost linearly with increasing electron beam load with a slope of approximately 80 K per $MW m^{-2}$. After neutron irradiation, this slope almost doubles,

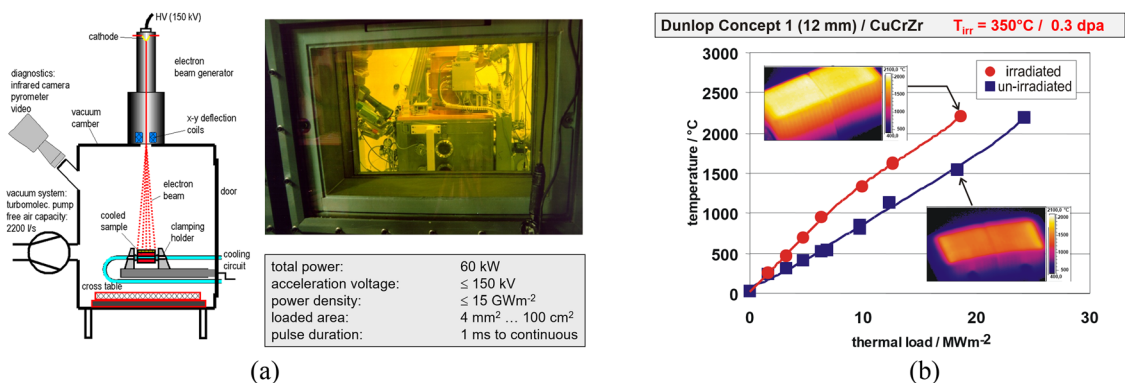


FIG. 20. (a) Schematic diagram from the electron beam test facility JUDITH 1 (left) and photograph from the test device inside the hot cell (right).³⁶ (b) High-heat-flux screening test up to absorbed power densities of 25 $MW m^{-2}$ in JUDITH 1 on an actively cooled monoblock target with CFC armor made from Dunlop Concept 1 and a CuCrZr coolant tube. The module has been tested before (blue curve) and after (red curve) neutron irradiation. The inserts are infrared images taken at the end of the 18 $MW m^{-2}$ heat pulses.⁷² Reprinted with permission from Linke *et al.*, Fusion Sci. Technol. **46**(1), 142–151 (2004). Copyright 2004 Taylor and Francis.

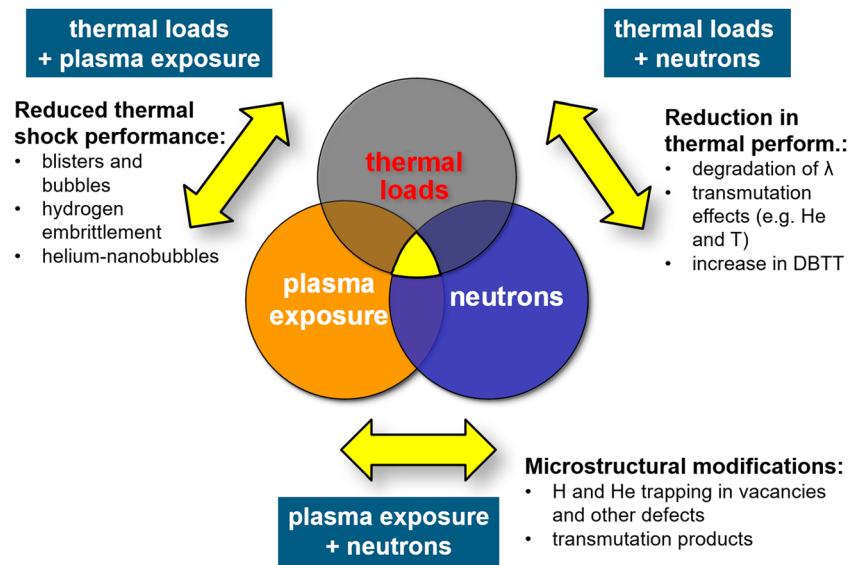


FIG. 21. Synergistic loading scenarios and important parameters with a strong impact on performance and lifetime of PFCs in future fusion reactors.

at least in the temperature range below 1000 °C, i.e., in a regime where recovery effects are less relevant. For higher heat loads (6 MW m^{-2} and above), some of the neutron-induced defects can be recovered, and the slope of the curve decreases considerably. Since the evaporation of carbon atoms from the heated surface increases dramatically above 2000 °C, the experiment had to be stopped at a heat load of 18 MW m^{-2} to avoid thermal erosion of the component and undesired contamination of the vacuum chamber and the diagnostic windows.

The thermal fatigue tests described in Fig. 8 have also been performed after neutron irradiation in the HFR reactor in Petten at a base temperature $T_{\text{irr}} = 700 \text{ °C}$ and a neutron fluence of 10^{25} n m^{-2} , which corresponds to damage rates of 1.0 dpa for carbon and 0.6 dpa for tungsten. After irradiation, the actively cooled components have been tested in JUDITH 1 under stepwise-increasing cyclic loads with 1000 fatigue cycles each. As has been pointed out above, carbon-armored PFCs are extremely sensitive to neutron-induced damage owing to their hexagonal lattice structure.

The CFC monoblock component could not be tested above 12 MW m^{-2} without any degradation of the module. This is due to the relatively low bulk temperature of the carbon material close to the coolant tube, which prevents recovery of irradiation-induced defects. For the flat tile design, this limit was somewhat higher (15 MW m^{-2}).

The tungsten monoblock module has demonstrated the best irradiation performance; here, the neutron-exposed PFC could tolerate ITER-like fluences of 10^{25} n m^{-2} without fatigue failure up to heat flux densities of 18 MW m^{-2} . These very promising results indicate that tungsten monoblock targets might also be a good choice for future fusion experiments with even higher neutron damage rates.

VI. SUMMARY AND CONCLUSIONS

The extremely harsh environment in future fusion reactors—high stationary and transient thermal loads, hydrogen and helium bombardment, 14 MeV neutrons—puts strong demands on the selection of

PFMs and the manufacture of actively cooled components with a long expected lifetime. Up to now, materials research in the field of thermonuclear fusion has been done primarily in laboratories and in test facilities that have focused primarily on individual effects only, such as thermal fatigue, thermal shocks during transient events, plasma exposure, and neutron irradiation tests. Today, emphasis is also laid on synergistic effects such as high thermal loads under plasma exposure or simultaneous thermal and neutron wall loads (see Fig. 21).

Synergies between thermal loads plus plasma exposure: Here, plasma-induced processes such as blister or bubble formation, hydrogen embrittlement, or the growth of He nanobubble layers or of fuzz on the plasma-exposed surface have a negative impact on resistance to intense thermal loads.

Synergies between thermal loads plus neutrons: Neutron-induced material degradation such as reduced thermal conductivity, transmutation effects, embrittlement, and increased ductile–brittle transition temperature have a strong impact on the high-heat-flux performance of wall components, both under steady-state conditions and under intense transients.

Synergies between plasma exposure plus neutrons: Research on this third synergism, namely, the interaction of plasma exposure with neutron-induced effects, has not been discussed here. In this area, future research should be directed toward the trapping of H and He in neutron-induced defects, the formation and influence of transmutation products, etc.

The results described in this paper indicate that material degradation is accelerated when synergistic effects are taken into consideration. Therefore, future experiments should also focus more strongly on these effects. New multipurpose test devices that enable simultaneous exposure with fusion-relevant ion fluxes and *in situ* thermal loading and that are well diagnosed are now available. The integration of these high-heat-flux and plasma devices into a powerful neutron source with a fusion-relevant energy spectrum would clearly go beyond current technical and financial limits. Alternatively, test

specimens (including miniaturized PFCs) must be irradiated in qualified neutron sources (material test reactors, spallation neutron sources, or later in IFMIF) to allow investigation by the above-mentioned multipurpose test devices.

The ideal, comprehensive testbed that enables simultaneous thermal loads, plasma exposure, and neutron irradiation (the yellow triangle in Fig. 21) is the D-T-burning fusion reactor itself. Although ongoing research is driven primarily by magnetic confinement fusion activities, in the near future it should also be adapted and applied to ICF-relevant conditions.

REFERENCES

- ¹Ch. Linsmeier *et al.*, “Material testing facilities and programs for plasma facing component testing,” *Nucl. Fusion* **57**, 092012 (2017).
- ²J. Linke, J. Compan, T. Hirai, G. Pintsuk, M. Rödiger, and K. Wittlich, “Materials for nuclear energy systems,” in *Proceedings of Forum 2008 of the World Academy of Ceramics, Chianciano Terme, Italy, July 5–8, 2008*, Ceramic Materials in Energy Systems for Sustainable Development, edited by L. Gauckler (Techna Group Srl, 2009), pp. 307–334.
- ³Y. Ueda *et al.*, “Baseline high heat flux and plasma facing materials for fusion,” *Nucl. Fusion* **57**, 092006 (2017).
- ⁴P. T. Lang *et al.*, “ELM control strategies and tools: Status and potential for ITER,” *Nucl. Fusion* **53**, 043004 (2013).
- ⁵A. Loarte *et al.*, “Characteristics of type I ELM energy and particle losses in existing devices and their extrapolation to ITER,” *Plasma Phys. Controlled Fusion* **45**, 1549 (2003).
- ⁶M. Merola *et al.*, “Overview and status of ITER internal components,” *Fusion Eng. Des.* **89**, 890 (2014).
- ⁷G. L. Kulcinski, “First wall protection schemes for inertial confinement fusion reactors,” *J. Nucl. Mater.* **85–86**(1), 87–97 (1979).
- ⁸V. Barabash *et al.*, “Armour materials for the ITER plasma facing components,” *Phys. Scr.* **T81**, 74 (1999).
- ⁹R. A. Pitts *et al.*, “A full tungsten divertor for ITER: Physics issues and design status,” *J. Nucl. Mater.* **438**, S48–S56 (2013).
- ¹⁰T. E. Evans, “ELM mitigation techniques,” *J. Nucl. Mater.* **438**, S11–S18 (2013).
- ¹¹T. Eich *et al.*, “Empirical scaling of inter-ELM power widths in ASDEX upgrade and JET,” *Nucl. Mater.* **438**, S72–S77 (2013).
- ¹²K. Wang *et al.*, “Morphologies of tungsten nanotendrils grown under helium exposure,” *Sci. Rep.* **7**, 42315 (2017).
- ¹³M. R. Gilbert and J.-C. Sublet, “Handbook of activation, transmutation, and radiation damage properties of the elements simulated using FISPACT-II & TENDL-2015; Magnetic fusion plants,” Report No. CCFE-R(16)36, September 2016.
- ¹⁴M. R. Gilbert, J.-Ch. Sublet, and S. L. Dudarev, “Spatial heterogeneity of tungsten transmutation in a fusion device,” *Nucl. Fusion* **57**(4), 044002 (2017).
- ¹⁵J. Linke, “Plasma facing materials and components for future fusion reactors,” in *Proceeding of the 12th Kudowa Summer School “Towards Fusion, to Energy,” Kudowa Zdroj, June 9–13, 2014*.
- ¹⁶M. Rieth, R. Doerner, A. Hasegawa, Y. Ueda, and M. Wirtz, “Behaviour of tungsten under irradiation and plasma interaction,” *J. Nucl. Mater.* **519**, 334–368 (2019).
- ¹⁷G. Pintsuk, I. Bobin-Vastra, S. Constans, P. Gavila, M. Rödiger, and B. Riccardi, “Qualification and post-mortem characterization of tungsten mock-ups exposed to cyclic high heat flux loading,” *Fusion Eng. Des.* **88**, 1858–1861 (2013).
- ¹⁸R. A. Pitts *et al.*, *J. Nucl. Mater.* **415**(1), S957–S964 (2011).
- ¹⁹Th. Loewenhoff *et al.*, “Impact of combined transient plasma/heat loads on tungsten performance below and above recrystallization temperature,” *Nucl. Fusion* **55**, 123004 (2015).
- ²⁰J. P. Gunn *et al.*, “Surface heat loads on the ITER divertor vertical targets,” *Nucl. Fusion* **57**, 046025 (2017).
- ²¹J. Schlosser *et al.*, “Technologies for ITER divertor vertical target plasma facing components,” *Nucl. Fusion* **45**(6), 512–518 (2005).
- ²²E. Visca *et al.*, “Hot radial pressing: An alternative technique for the manufacturing of plasma-facing components,” *Fusion Eng. Des.* **75**, 485–489 (2005).
- ²³A. Herrmann *et al.*, “Experiences with a solid tungsten divertor in ASDEX upgrade,” *Nucl. Mater. Energy* **12**, 205–209 (2017).
- ²⁴C. Thomser *et al.*, “Plasma facing materials for the JET ITER-like wall,” *Fusion Sci. Technol.* **62**(1), 1–8 (2012).
- ²⁵T. Hirai *et al.*, “Use of tungsten material for the ITER divertor,” *Nucl. Mater. Energy* **9**, 616–622 (2016).
- ²⁶A. R. Raffray *et al.*, *Nucl. Fusion* **54**, 033004 (2014).
- ²⁷M. Wirtz, I. Uytendhouwen, V. Barabash, F. Escourbiac, T. Hirai, J. Linke, Th. Loewenhoff, S. Panayotis, and G. Pintsuk, “Material properties and their influence on the behaviour of tungsten as plasma facing material,” *Nucl. Fusion* **57**, 066018 (2017).
- ²⁸Z. Zhou, Y. Ma, J. Du, and J. Linke, “Fabrication and characterization of ultra-fine-grained tungsten by resistance sintering under ultra-high pressure,” *Mater. Sci. Eng., A* **505**, 131–135 (2009).
- ²⁹Ch. Linsmeier *et al.*, “Development of advanced high heat flux and plasma-facing materials,” *Nucl. Fusion* **57**, 092007 (2017).
- ³⁰J. W. Coenen *et al.*, “Materials for DEMO and reactor applications—Boundary conditions and new concepts,” *Phys. Scr.* **T167**, 014002 (2016).
- ³¹G. De Temmerman, T. Hirai, and R. A. Pitts, “The influence of plasma-surface interaction on the performance of tungsten at the ITER divertor vertical targets,” *Plasma Phys. Controlled Fusion* **60**, 044018 (2018).
- ³²G. De Temmerman, “High heat flux capabilities of the magnum-PSI linear plasma device,” *Fusion Eng. Des.* **88**, 483–487 (2013).
- ³³J. H. Yu, G. De Temmerman, R. P. Doerner, and M. A. van den Berg, “Study of temporal pulse shape effects on W using simulations and laser heating,” *Phys. Scr.* **T167**, 014033 (2016).
- ³⁴J. Ahlf *et al.*, “The HFR Petten as a test bed for fusion materials and components,” *J. Nucl. Mater.* **212–215**(B), 1635–1639 (1994).
- ³⁵T. Hirai *et al.*, “ITER relevant high heat flux testing on plasma facing surfaces,” *Mater. Trans.* **46**(3), 412–424 (2005).
- ³⁶R. Duwe *et al.*, *Fusion Technol.* **1994**, 355–358 (1995).
- ³⁷A. Schmidt *et al.*, *Fusion Eng. Des.* **83**(7–9), 1108–1113 (2008).
- ³⁸P. Majerus *et al.*, *Fusion Eng. Des.* **75–79**, 365–369 (2005).
- ³⁹G. Pintsuk, “Tungsten as a plasma-facing material,” *Compr. Nucl. Mater.* **4**, 551–581 (2012). Reference Module in Materials Science and Materials Engineering.
- ⁴⁰A. Zhitlukhin *et al.*, “Effect of ELMS on ITER armour materials,” *J. Nucl. Mater.* **363–365**, 301–307 (2007).
- ⁴¹B. Bazylev *et al.*, “Experimental validation of 3D simulations of tungsten melt erosion under ITER-like transient loads,” in *18th International Conference on Plasma Surface Interactions in Controlled Fusion Devices*, Toledo, Spain, May 26–30, 2008.
- ⁴²H. Greuner *et al.*, “Surface morphology changes of tungsten exposed to high heat loading with mixed hydrogen/helium beams,” *J. Nucl. Mater.* **455**, 681 (2014).
- ⁴³M. Wirtz, J. Linke, Th. Loewenhoff, G. Pintsuk, and I. Uytendhouwen, “Thermal shock tests to qualify different tungsten grades as plasma facing material,” *Phys. Scr.* **T167**, 014015 (2016).
- ⁴⁴M. Wirtz *et al.*, “Transient heat load challenges for plasma-facing materials during long-term operation,” *Nucl. Mater. Energy* **12**, 148–155 (2017).
- ⁴⁵J. Linke *et al.*, “Performance of different tungsten grades under transient thermal loads,” *Nucl. Fusion* **51**, 073017 (2011).
- ⁴⁶Th. Loewenhoff *et al.*, *Phys. Scr.* **T145**, 014057 (2011).
- ⁴⁷Th. Loewenhoff *et al.*, *Fusion Eng. Des.* **87**, 1201–1205 (2012).
- ⁴⁸K. Wittlich *et al.*, “Damage structure in divertor armor materials exposed to multiple ITER relevant ELM loads,” *Fusion Eng. Des.* **84**, 1982–1986 (2009).
- ⁴⁹J. Compan, T. Renk, T. Hirai, and J. Linke, “Reduction of preferential erosion of carbon fibre composites under intense transient heat pulses,” *Phys. Scr.* **T128**, 246–249 (2007).
- ⁵⁰J. Linke, “Plasma facing materials and components for future fusion devices—development, characterization and performance under fusion specific loading conditions,” *Phys. Scr.* **T123**, 45–53 (2006).

- ⁵¹J. Linke, "High heat flux performance of plasma facing materials and components under service conditions in future fusion reactors," *Trans. Fusion Sci. Technol.* **53**, 278–287 (2008).
- ⁵²M. Roedig *et al.*, *J. Nucl. Mater.* **417**, 761–764 (2011).
- ⁵³G. Pintsuk, W. Kühnlein, J. Linke, and M. Rödig, "Investigation of tungsten and beryllium behaviour under short transient events," *Fusion Eng. Des.* **82**, 1720–1729 (2007).
- ⁵⁴B. Spilker *et al.*, *Nucl. Mater. Energy* **9**, 145–152 (2016).
- ⁵⁵B. Spilker *et al.*, "Experimental study of ELM-like heat loading on beryllium under ITER operational conditions," *Phys. Scr.* **T167**, 014024 (2016).
- ⁵⁶B. Spilker *et al.*, "High pulse number transient heat loads on beryllium," *Nucl. Mater. Energy* **12**, 1184–1188 (2017).
- ⁵⁷B. Spilker *et al.*, "Performance estimation of beryllium under ITER relevant transient thermal loads," *Nucl. Mater. Energy* **18**, 291–296 (2019).
- ⁵⁸A. Hassanein and I. Konkashbaev, "Lifetime evaluation of plasma-facing materials during a tokamak disruption," *J. Nucl. Mater.* **233-237**, 713–717 (1996).
- ⁵⁹I. S. Landman, S. E. Pestchanyi, Y. Igitkhanov, and R. Pitts, "Two-dimensional modeling of disruption mitigation by gas injection," *Fusion Eng. Des.* **86**(9-11), 1616–1619 (2011).
- ⁶⁰E. Martin, G. Camus, J. Schlosser, and G. Chevet, "Damage modelling in plasma facing components," *J. Nucl. Mater.* **386-388**, 747–750 (2009).
- ⁶¹S. J. Zinkle and J. T. Busby, "Structural materials for fission & fusion energy," *Mater. Today* **12**(11), 12–19 (2009).
- ⁶²R. P. Doerner, M. J. Baldwin, T. C. Lynch, and J. H. Yu, "Retention in tungsten resulting from extremely high fluence plasma exposure," *Nucl. Mater. Energy* **9**, 89–92 (2016).
- ⁶³M. Wirtz, A. Kreter, J. Linke, Th. Loewenhoff, G. Pintsuk, G. Sergienko, I. Stuedel, B. Unterberg, and E. Wessel, "High pulse number thermal shock tests on tungsten with steady state particle background," *Phys. Scr.* **T170**, 014066 (2017).
- ⁶⁴G. De Temmerman, T. W. Morgan, G. G. van Eden, T. de Kruijff, M. Wirtz, J. Matejcek, T. Chraska, R. A. Pitts, and G. M. Wright, "Effect of high-flux H/He plasma exposure on tungsten damage due to transient heat loads," *J. Nucl. Mater.* **463**, 198–201 (2015).
- ⁶⁵A. Kreter *et al.*, "Linear plasma device PSI-2 for plasma-material interaction studies," *Fusion Sci. Technol.* **68**, 8–14 (2015).
- ⁶⁶M. Wirtz *et al.*, *Nucl. Mater. Energy* **9**, 177–180 (2016).
- ⁶⁷A. Huber *et al.*, "Investigation of the impact of transient heat loads applied by laser irradiation on ITER-grade tungsten," *Phys. Scr.* **T159**, 014005 (2014).
- ⁶⁸G. Federici *et al.*, "Overview of the design approach and prioritization of R&D activities towards an EU DEMO," *Fusion Eng. Des.* **109-111**, 1464–1474 (2016).
- ⁶⁹G. Pintsuk *et al.*, "High heat flux testing of first wall mock-ups with and without neutron irradiation," *Nucl. Mater. Energy* **9**, 41–45 (2016).
- ⁷⁰T. Tanabe, "Radiation damage of graphite - degradation of material parameters and defect structures," *Phys. Scr.* **T64**, 7–16 (1996).
- ⁷¹J. Linke, P. Lorenzetto, P. Majerus, M. Merola, D. Pitzer, and M. Rödig, "EU development of high heat flux components," *Fusion Sci. Technol.* **47**(3), 678 (2005).
- ⁷²J. Linke, T. Hirai, M. Rödig, and L. A. Singheiser, "Performance of plasma-facing materials under intense thermal loads in tokamaks and stellarators," *Fusion Sci. Technol.* **46**(1), 142–151 (2004).